phys. stat. sol. (a) **91**, 465 (1985)

Subject classification: 1.1; 1.4; 10

*Institut für Festkörperphysik und Elektronenmikroskopie der Akademie der Wissenschaften der DDR, Halle (Saale)*[1])

# Calculated Defocus Diffraction Contrast and Lattice Fringe Imaging of Small Crystal Defects

By

K. SCHEERSCHMIDT and R. HILLEBRAND

Dedicated to Prof. Dr. Dr. h. c. Dr. E. h. P. GÖRLICH on the occasion of his 80th birthday, also in the name of Prof. H. Bethge, Prof. V. Schmidt, and Prof. J. Heydenreich

In transmission electron microscopy of crystal lattice defects, the imaging of details smaller than a few nanometres requires the consideration of the electron optical imaging process in addition to the study of the interaction between electron beam and crystal. A method is described combining the calculation of diffraction contrast amplitudes with the Fourier transformation formalism for simulating bright- or dark-field diffraction contrasts and lattice fringe images of arbitrarily small crystal defects. Simulated images are presented demonstrating the applicability of this method and the significance of microscope aberrations for the interpretation of diffraction contrast and lattice fringe images.

Die Erfassung von Kontrastdetails kleiner als einige Nanometer bei der Kristallgitter-Defektabbildung im Transmissionselektronenmikroskop erfordert die gleichzeitige Untersuchung des elektronenoptischen Prozesses und des Wechselwirkungsprozesses zwischen Elektronenstrahl und Kristall. Es wird eine Methode beschrieben, die die Kombination der Berechnung der Beugungskontrastamplituden mit dem Formalismus der Fouriertransformation ermöglicht, um Hellfeld- oder Dunkelfeld-Beugungskontrast und Netzebenenabbildung für beliebig klein Kristalldefekte zu simulieren. Es werden simulierte Abbildungen kleiner Kristalldefekte untersucht, um die Anwendbarkeit der entwickelten Methode zu demonstrieren und die Bedeutung der elektronenoptischen Aberrationen für die Interpretation von Beugungskontrast und Netzebenenabbildungen aufzuzeigen.

## 1. Introduction

In transmission electron microscopy the nature of small crystal lattice defects can be analysed by the well-established method of diffraction contrast imaging. Additional supporting information can be obtained by lattice fringe and multi-beam images.

If, however, the above techniques are applied to the analysis of high-resolution image details smaller than about a nanometer, the imaging process itself becomes more and more important, placing extra demands on the interpretation of the images [1]. The microscope aberrations modify the black-white patterns of the diffraction contrast and create a blurring of the lattice fringes distorted by a crystal defect. So, for instance, out-of-focus diffraction contrast of small point defect clusters creates black-white figures even under conditions where otherwise only black lobe contrast might be expected [2]. On the other hand, the outward or inward bending of fringes caused by dislocation loops or small precipitates no longer guarantees unequivocally the interstitial or vacancy nature of the defects [3]. Nevertheless, comprehensive analyses of the defect images and lattice fringe distortions including the microscope

[1]) Weinberg 2, DDR-4010 Halle (Saale), GDR.

aberrations should yield information on the local defect structure. A systematic study of all the relevant parameters (e.g. foil thickness $t$, defect depth position $t_0$, crystal orientation given here by the excitation error $s_g$, defocus $\Delta$, spherical aberration $C_s$, accelerating voltage $U$) and the investigation of the correlation between the nature of the defect and the fringe distortion obtained is only possible if the entire image (diffraction contrast or lattice fringes) of the small defect is considered. Therefore, for example, the analysis of the phase profiles in [3] should be replaced by simulated lattice fringe images to decide whether the fringes are terminated or shifted, or whether the termination is annihilated over larger defect regions.

To enable this simulation of complete two-dimensional lattice fringe images, a method is outlined to combine the calculation of diffraction contrast amplitudes with the calculation of the imaging process in the microscope [4]. This technique, of course, also allows the computation of the defocus diffraction contrast of crystal defects. The general formulation of these procedures extends the applicability and yields quantitative results in addition to analytical approximation [3, 5 to 7].

## 2. Method

A number of approximations has been elaborated to describe mathematically diffraction by crystals containing defects. These methods can be divided mainly into two groups, the direct space approaches and the calculations in reciprocal space. As shown in [1], the reciprocal space methods use the concept of periodic continuation and therefore yield good approximations solely for very small defects. Furthermore, it is concluded that the direct space methods without column approximation are valid irrespective of the degree of distortion, and that for any given level of resolution and degree of distortion, the column approximation is valid for a sufficiently thin crystal. Therefore, in the present work the interaction process is calculated using the direct space method of column approximation, whereas the imaging process is described numerically by Fourier analysis and synthesis suitably modified by a contrast transfer function.

### *2.1 Calculation of diffraction amplitudes*

The use of the column approximation enables the basic equations of the direct space approach to be reduced to the standard set of differential scattering equations [8, 9]

$$\frac{\mathrm{d}}{\mathrm{d}z}\Phi_g(\boldsymbol{R}, z) = 2\pi i\beta'_g\,\Phi_g(\boldsymbol{R}, z) + \sum_h A_{gh}\Phi_h(\boldsymbol{R}, z)\,. \tag{1}$$

Here $\Phi_g$ denotes the amplitudes for plane wave expansion of the wave function and $\Phi_g(\boldsymbol{R}, t)$ describes the outgoing plane vacuum wave in $\boldsymbol{k} + \boldsymbol{g}$ direction at the exit crystal surface, i.e. for a reflection $\boldsymbol{g}$, where $\boldsymbol{k}$ is the incident beam direction, corrected for refraction ($|\boldsymbol{k}| \approx K_z \approx 1/\lambda$, wavelength $\lambda$, $\boldsymbol{r} = (\boldsymbol{R}, z)$, $\boldsymbol{R}$ column position). The scattering matrix $A_{gh} = 2\pi i(s_g\delta_{gh} + V_{g-h}/2K_z)$ describes the potential of the perfect lattice by the structure amplitude $V_g$ and the orientation of the crystal by the excitation errors $s_g$ (relative orientation between $\boldsymbol{k}$ and the Laue zone of $\boldsymbol{g}$). The dependence on the crystal defect is determined by the disturbance $\beta'_g = (\mathrm{d}/\mathrm{d}z)\,(\boldsymbol{g}\cdot\boldsymbol{u}(\boldsymbol{R}, z))$ which is the gradient of the displacement field component parallel to the diffraction vector $\boldsymbol{g}$.

The coordinates of (1) can be normalized to the extinction distances $\xi_g = K_z/|V_g|$ by introducing the dimensionless deviation parameters $w_g = \xi_g s_g$, as commonly used

in the two-beam situation. For describing the absorption, in a way similar to that used for $\xi_g$ the normal and anomalous absorption parameters $\xi_0'$ and $\xi_g'$, respectively, are introduced replacing $V_g$ by the optical potential. The normal absorption can be handled by transformation; in the present paper for the sake of simplicity it is included in (1).

The numerical solution of the set of differential equations (1) is treated here by a Runge-Kutta integration procedure or by a modified Thölèn method and by using interpolation procedures (see Section 2.4) as in [10], since the method of "generalized cross sections" cannot be used for the non-straight defects considered here. A transformation of the differential equation system for reducing its order is also not applicable here because of the lack of the phase information necessary for lattice fringe imaging (see, for example [11]).

The present authors prefer numerical methods instead of the analytical description [3] using Katerbau's matrices [5] since for the quantitative analysis of high-resolution details the "mean defect parameters" are insufficient and have also to be specified numerically for each column. But, for extending the present results to larger parameter ranges, the analytical methods with their comprehensive physical treatment of the contrast mechanisms are very helpful.

### *2.2 Construction of the displacement fields*

For calculating the displacement gradient $\beta_g'$, idealized defect configurations and simplified elastic approximations are used, since these assumptions sufficiently explain the general features of lattice fringe contrast. But for interpreting particular experimental problems the calculation can be extended to arbitrarily complex displacement fields; this will be considered in subsequent papers.

In the present work, the elastic displacement field $\boldsymbol{u}$ of a straight dislocation is calculated by the well-known approximation for isotropic media where the displacement field of grain boundaries is built up by pile-up configurations of straight dislocations. For considering the surface relaxation, which is of main importance in or near the edge-on position of the dislocations, in a first approximation the rotation and the change in the lattice spacing caused by the dislocations are included in the $\beta_g'$-calculation (model of Bonse reported in [12]). This model will be called "lattice rotation model" which is determined by the additional displacement gradient in the direction of the diffraction vector ($\theta_B$ Bragg angle),

$$\beta_g' = \left(\frac{\partial}{\partial z} + \theta_B \frac{\partial}{\partial r_g}\right) \boldsymbol{g} \cdot \boldsymbol{u} \ . \tag{2}$$

A more complete treatment of surface relaxation for dislocations in exact end-on position is employed based on the calculations of Tunstall et al. [13].

For the calculation of curved dislocations, it is normally sufficient to approximate the dislocation line by suitably chosen polygonal dislocation configurations [10]. In this way the displacement field of a hexagonal dislocation loop is constructed by the superposition of six angular dislocations [4, 10, 11, 14]. Subsequent papers will deal with the problems of improved models for dislocations seen end-on, precipitates, as well as the range of applications which are of practical interest.

The case of wedge-shaped crystals (see Fig. 7) has been computed by changing the boundary conditions for the integration procedure corresponding to the slope of the surfaces.

### *2.3 Investigation of the phases of diffracted waves*

The interaction of the electrons with the crystal leads to the scattered outgoing wave field

$$\psi(\boldsymbol{r}) = \psi_e(\boldsymbol{R})\, e^{2\pi i \boldsymbol{k}\boldsymbol{r}} \tag{3}$$

at the exit crystal surface $z = t$ with

$$\psi_e(\boldsymbol{R}) = \sum_g \Phi_g(\boldsymbol{R}, t)\, e^{2\pi i \boldsymbol{g}\boldsymbol{R}} . \tag{4}$$

The complex amplitude functions $\Phi_g = \Phi_g^{re} + i\Phi_g^{im}$ characterize the plane waves in the $\boldsymbol{k} + \boldsymbol{g}$ direction and therefore the reflection intensities in the back focal plane of the objective lens. The amplitudes $\Phi_g$ are functions of the position $\boldsymbol{R}$ if the crystal is imperfect or bent; they can be represented by a modulus $T_g$ and a phase $\varphi_g$ yielding

$$\Phi_g(\boldsymbol{R}, t) = T_g(\boldsymbol{R}, t)\, e^{i\varphi_g(\boldsymbol{R}, t)} . \tag{5}$$

Formally the "plane" image wave function can be expressed by the convolution

$$\psi_i(\boldsymbol{R}) = P(\boldsymbol{R}) * \psi_e(\boldsymbol{R}) \tag{6}$$

with the point-spread function $P(\boldsymbol{R})$ which is the Fourier transform of the transfer function of the electron microscope [1]. The practical realization of (6) is described in Section 2.4. The image intensity is then

$$I(\boldsymbol{R}) = |\psi_i(\boldsymbol{R})|^2 . \tag{7}$$

In imaging with aberration-free and in-focus conditions, called here "ideal imaging", the transfer function is equivalent to the aperture function, and therefore the convolution consists in a restriction of the summation in (4) to only those reflections which pass through the objective aperture. Thus

$$I_{BF} = |\Phi_0|^2 = T_0^2 , \tag{8a}$$

$$I_{DF} = |\Phi_g|^2 = T_g^2 , \tag{8b}$$

and

$$I_{LF} = |\sum_g \Phi_g\, e^{2\pi i \boldsymbol{g}\boldsymbol{R}}|^2 = |\sum_g T_g\, e^{2\pi i \boldsymbol{g}\boldsymbol{R} + i\varphi_g}|^2$$
$$= \sum_g T_g^2 + \sum_{g \neq h} \sum T_g T_h \cos\left[2\pi(\boldsymbol{g} - \boldsymbol{h})\,\boldsymbol{R} + \varphi_g - \varphi_h\right] \tag{8c}$$

describe the ideal image contrast of bright-field and dark-field diffraction and lattice fringes, respectively. This shows that here the phases $\varphi_g$ with their differences $\delta\varphi = \varphi_g - \varphi_h$ are of interest only in lattice fringe contrast.

If, however, the aberration of the imaging process cannot be neglected, as occurs at higher resolution (see the following numerical treatment), the phases $\varphi_g$ play an important role even in diffraction contrast imaging. In first-order approximations (see Appendix A and [7]), the diffraction intensities can be described by

$$I_{BF,DF}^{CTF} = [1 + q(\boldsymbol{R})]\; I_{BF,DF}(\boldsymbol{R} + \boldsymbol{\delta}(\boldsymbol{R})) , \tag{9a}$$

whereas for lattice fringe imaging one obtains

$$I_{LF}^{CTF} = \sum_g T_g^2 + \sum_{g \neq h} \sum T_g T_h \cos\left[2\pi(\boldsymbol{g} - \boldsymbol{h})\,\boldsymbol{R} + \varphi_g - \varphi_h + \chi(\boldsymbol{g}) - \chi(\boldsymbol{h})\right] . \tag{9b}$$

Amplification factor $q(\boldsymbol{R})$ and image shift $\boldsymbol{\delta}(\boldsymbol{R})$ for diffraction contrast as well as the direct additional phase shift of lattice fringes caused by the contrast transfer function (CTF) in the form of $\chi(\boldsymbol{g})$ are discussed in Appendix A.

Two-beam diffraction at a thin perfect crystal where absorption is neglected yields

$$T_0 = \sqrt{1 - T_g^2}\,, \qquad T_g = \frac{1}{\sqrt{1 + w^2}} \sin\left(\frac{\pi t}{\xi_g}\sqrt{1 + w^2}\right),$$

$$\cot(\varphi_g - \varphi_0) = -\frac{w}{\sqrt{1 + w^2}} \tan\left(\frac{\pi t}{\xi_g}\sqrt{1 + w^2}\right) \tag{10}$$

(for the derivation of (10) and more general expressions including absorption, see Appendix B). $T_0$ and $T_g$ describe the well-known Bragg extinction contours and the thickness fringes at $w = 0$ and $t/\xi_g = m/\sqrt{1 + w^2}$, respectively. They also characterize the visibility of lattice fringes according to (9b), resulting in a minimal visibility for $t = m\xi_g/2\sqrt{1 + w^2}$ and a maximal visibility for $\sin(\pi t\sqrt{(1 + w^2)}/\xi_g) = \sqrt{1 + w^2/2})$. The more important phase differences of (10) characterize directly the displacement of the fringes due to $w$ and $t$. A sign reversal of $\cot(\varphi_g - \varphi_0)$ causes an increase or decrease of $\delta\varphi$ by $\pi$. This increase or decrease describes a strong bending or shifting of the lattice fringes which should occur (cf. (10)) at Bragg contours or thickness fringes (showing results similar to those in [15]). At $t = 0$ the phase difference is $\delta\varphi = \pi/2$ and, besides in places of discontinuous $\delta\varphi$, the approximation $\delta\varphi \approx \pi s t$ holds.

For non-perfect crystals, to first-order approximation, $w$ can be replaced by $w + \xi_g\beta_g'$ in (10), or as Appendix B also shows, the phase difference $\delta\varphi$ is replaced by

$$\delta\varphi = \varphi_g - \varphi_0 = 2\pi[\beta_g(t) - \beta_g(0)] - \frac{w}{\sqrt{1 + w^2}} \tan\left(\frac{\pi t}{\xi_g}\sqrt{1 + w^2}\right). \tag{11}$$

These considerations explain the effect of crystal defects on lattice fringe contrast in first-order approximation, extrapolating the behaviour of perfect specimens. A more quantitative analysis requires a more detailed knowledge of modulus and phases implying a numerical calculation.

As to the mechanism of lattice fringe distortions Fig. 1 shows numerically calculated phase differences $\delta\varphi = \varphi_g - \varphi_0$ using (1) for the two-beam situation and the displacement field of a screw dislocation inclined at 30° to the foil surface. The coordinates $\boldsymbol{R} = (x, y)$ of the phase diagram indicate the position of the columns of integration where the projection of the screw coincides with the $y$-axis. Thus, $x$ describes the distance from the dislocation line, and $y$ can be interpreted in terms of the depth position of the dislocation.

The behaviour of $\delta\varphi$ predicted approximately can be confirmed by analytical considerations. Furthermore, for increasing the distances the displacement field acts as a discontinuity which explains the phase shift of $\pm\pi$ from $x = -\infty$ to $\infty$. Changing the depth position $y$ implies the reversal of the sign of the phase shift, so that a transition region exists (see dashed lines) characterizing a $2\pi$-discontinuity. In the neighbourhood of this phase gap, in the corresponding lattice fringe patterns, a terminated fringe occurs because of the ambiguity of the phase relations. For the practical application of the real microscopic imaging process it becomes obvious that the approximately known phases and modules can describe only qualitatively the properties of image contrast.

### *2.4 Calculation of the imaging process*

The imaging process is fully described by the convolution given in (6). In practice, however, the convolution theorem is employed. Thus for the given diffraction angles (small-angle approximation, linearity) the imaging procedure may be described by a sequence of Fourier transforms ($\mathcal{F}$, $\mathcal{F}^{-1}$) [11]. As to the objective lens, the wave

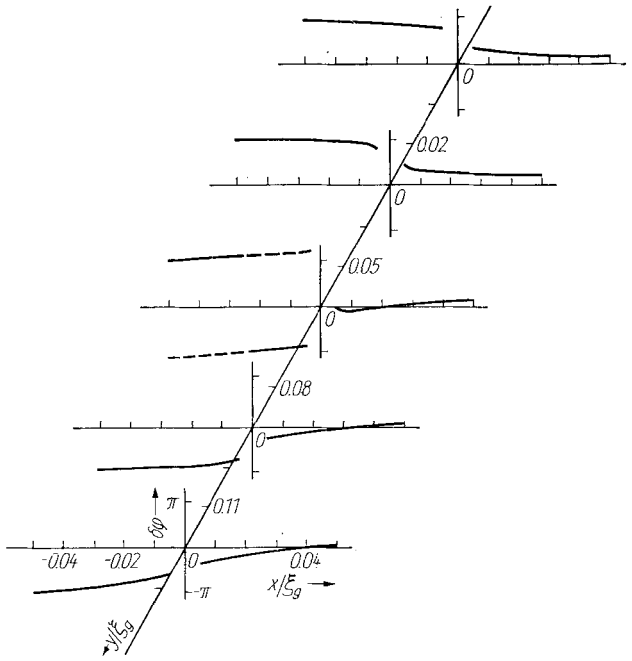


Fig. 1. Set of diagrams showing phase differences $\delta\varphi = \varphi_g - \varphi_0$ as a function of column position $\boldsymbol{R} = (x, y)$ for an inclined screw dislocation. Parameters: $\boldsymbol{g} = (111)$, $\boldsymbol{b} = \frac{1}{2}[011]$, $\boldsymbol{e} = [\bar{1}10]$, $t = \xi_g/4$ ($\xi_g$ of Ge; the dashed curves indicate the phase ambiguity of $2\pi$ characterizing a terminated fringe at $y = 0.06$)

function in the back focal plane, i.e. the diffraction pattern, is given by

$$\psi_d(\boldsymbol{\varrho}) = \mathcal{F}[\psi_e(\boldsymbol{R})] . \tag{12}$$

The frequency spectrum $\psi_d(\boldsymbol{\varrho})$ consists of sharp reflections at $\boldsymbol{\varrho} = \boldsymbol{g}_i$ for perfect crystals. It shows a fine structure surrounding all reflections $\boldsymbol{g}_i$ due to the local variation in $\Phi_g(\boldsymbol{R})$ due to the lattice defects. Under the actual experimental conditions $\psi_d(\boldsymbol{\varrho})$ is multiplied by a binary aperture function $A(\boldsymbol{\varrho})$. The electron microscope aberrations are considered in the contrast transfer function (CTF) [11] with special reference to the point-spread properties $P(\boldsymbol{R})$ of the microscope $\mathrm{CTF}(\boldsymbol{\varrho}) = \mathcal{F}[P(\boldsymbol{R})]$ in reciprocal space

$$\psi_{d'}(\boldsymbol{\varrho}) = \psi_d(\boldsymbol{\varrho})\, A(\boldsymbol{\varrho})\, e^{-i\chi(\varrho)-E(\varrho)} ; \qquad \chi(\boldsymbol{\varrho}) = \pi\lambda[\Delta\varrho^2 - C_s\lambda^3\varrho^4/2] , \tag{13}$$

where $E$ represents the partial coherence by an envelope function, which describes the resulting spread of defocus. The inverse Fourier transform of the modified spatial amplitudes $\psi_{d'}(\boldsymbol{\varrho})$ provides the wave function in the image plane

$$\psi_i(\boldsymbol{R}) = \mathcal{F}^{-1}[\psi_{d'}(\boldsymbol{\varrho})] . \tag{14}$$

The intensity distribution of the final image, which should be matched by the simulation procedure, is then given by (7). For distinguishing the blurring influence of microscopic aberrations from the direct specimen signal, perfect contrast transfer ($C_s = 0$, $\Delta = 0$) is assumed in some tables of calculated patterns. The application of (12) to (14) is realized numerically using a fast Fourier transformation which assumes a knowledge of the complex amplitudes $\Phi_g(\boldsymbol{R}_{lm})$ at the exit crystal surface for all

$2^{n_x}$ rows ($l = 1, 2, \ldots, 2^{n_x}$) and $2^{n_y}$ columns ($m = 1, 2, \ldots, 2^{n_y}$) of image pixels with coordinates $\boldsymbol{R}_{lm} = (x_0 + l\,\delta x, y_0 + m\,\delta y)$. For saving computation time, however, the numerical calculation of $\Phi_g(\boldsymbol{R}_{lm})$ by integrating the differential equation system (1) is treated only for about 20% of the pixels; their completion is carried out by interpolation. The integrated pixels act as pivot points building up the complete image by two-dimensional linear interpolation of the image intensity. Thereby, the intensity of each interpolated pixel is calculated by evaluating two different groups of pivot points. It is replaced by the mean value, if the interpolated values are comparable. The error limits allowable are fixed by test calculations and determine the interpolation accuracy. As the integration of (1) is the stage that is most time-consuming the interpolation procedure is extended to the interpolation of the complex amplitudes.

While the independent interpolation of real and imaginary parts of $\Phi_g$, on the one hand, describes the phase behaviour more accurately, the interpolation of modulus and phases, on the other hand, results in smoother diffraction contrast images (see Appendix C). In the former case, the modulus shows an irregular behaviour at pixels with strong phase oscillations. In the latter case, i.e. if both modulus and phases are interpolated, sudden phase changes can be smoothed out, and due to the periodicity ($2\pi n$) of the phases, irregular phase discontinuities can be additionally generated.

A physically consistent interpolation procedure for calculating both the diffraction contrast and the lattice fringe imaging must reproduce the intensities as well as the phases without irregularities. Therefore, in the present paper both the interpolation procedures are combined in such way that the phases are determined by independently interpolating the real and imaginary parts. The modulus, however, is corrected using the interpolation formulae of the intensities. Thereby, the error criterion of intensity interpolation also controls the interpolation of the modulus. The extensively discussed interpolation of complex amplitudes is summarized considering the calculated diffraction contrast and lattice fringe images of a dislocation seen end-on in Au (lattice rotation model).

In Fig. 2 the interpolation of modulus/phase functions (Fig. 2a to c) is compared with that of real/imaginary parts with corrected modulus (Fig. 2d to f). The ideal bright-field images do not show significant differences, which proves that the independent interpolation of real and imaginary parts corrected by the modulus yields the same results as the intensity interpolation for pure diffraction contrast. Furthermore, the phase interpolation yields additional phase discontinuities creating virtual structures in the defocused bright-field and lattice fringe imaging. These virtual structures disappear (Fig. 2e and f) using the interpolation of real and imaginary parts corrected by the modulus (see Appendix C). If the defocused images (Fig. 2b, e) are compared with the ideal bright-field contrast (Fig. 2a, d), the present interpolation procedure seems satisfactory, since the rough contrast features of the bright-field are reproduced only in Fig. 2e despite the microscope aberrations. The absence of any fringe distortions in Fig. 2f, which has been discussed in connection with Fig. 4, is a direct result of the displacement field approximation.

Besides the problem of interpolating complex amplitudes, the question of the order of interpolation and the selection of pivot points have to be discussed. Using linear interpolation, the loss of accuracy in comparison with higher-order algorithms can be compensated by applying suitable interpolation error limits, because an accuracy within one grey level is sufficient for the final image. Furthermore, the procedure of bilinear interpolation calculating the arithmetic mean of two-point or three-point pivot groups will decrease the checker-board effect in a similar way to that of reducing a four-point interpolation to a three-point one [16].

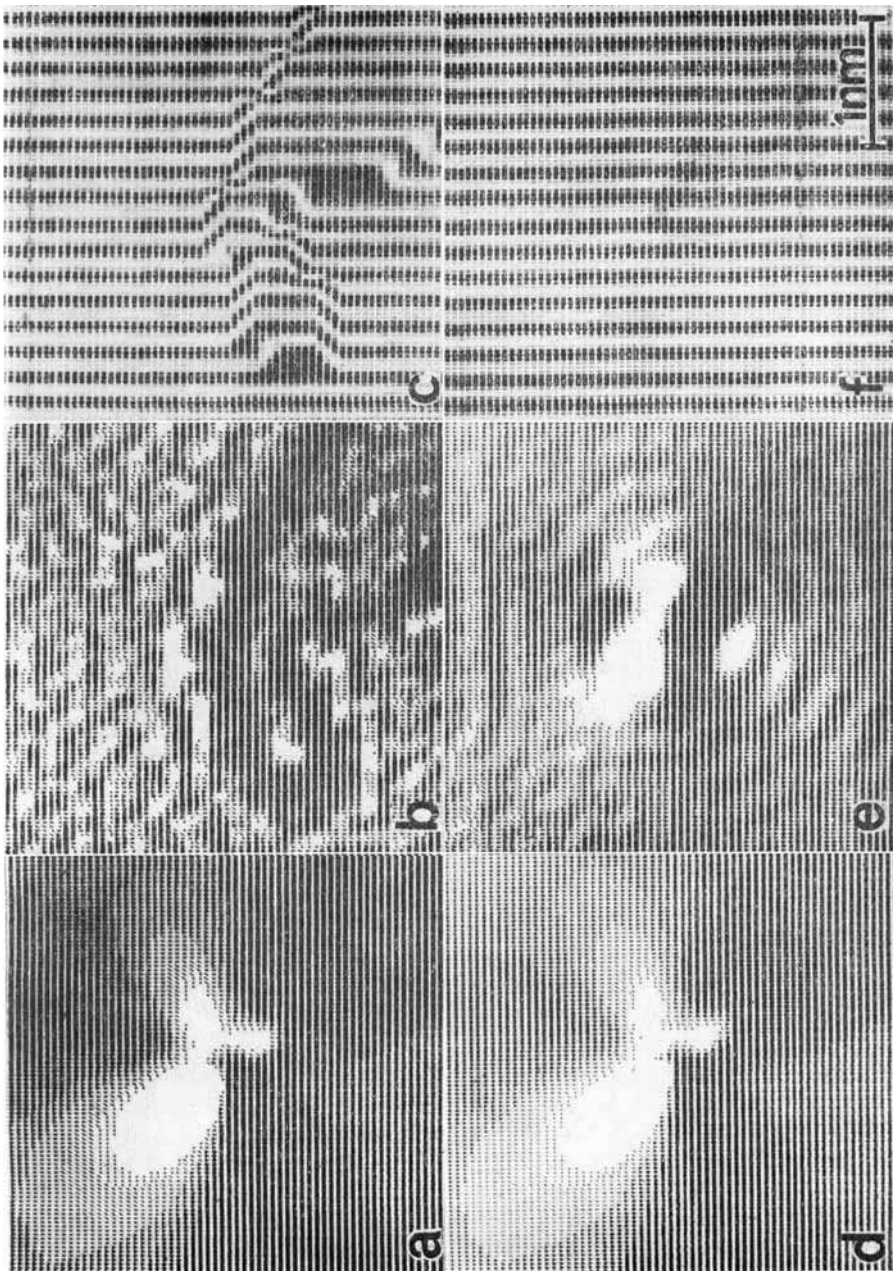


Fig. 2. Comparison of modulus/phase interpolation, a) to c), with modulus-corrected real/imaginary part interpolation, d) to f), for a dislocation seen end-on, a) and d) ideal and b) and e) aberrated bright-field contrast as well as c) and f) lattice fringe images. Parameters: $\boldsymbol{g} = (200)$, $\boldsymbol{b} \approx [100]$, $\boldsymbol{e} = [001]$, $t = 3{,}45_g$, $w = 0$

## 3. Results

The image simulation procedure described in Section 2 is now applied to study the mechanism of crystal defect contrast. The investigation is concerned with the influence of microscope aberrations on diffraction contrast (Section 3.1) as well as on lattice fringe (Section 3.2) imaging. Thereby various crystal defects are presupposed for testing the applicability of the present simulation method considering both processes of interaction and imaging.

### *3.1 Defocus diffraction contrast*

The influence of the electron microscope imaging process on the bright-field contrast of prismatic loops in Au specimens is shown in the series of Fig. 3. The hexagonal loops ($\boldsymbol{n} = [11\bar{1}]$), which are built up by six angular dislocations ($\boldsymbol{b} = \frac{1}{3}(1\bar{1}1)$) are imaged using the [110] beam direction. In the upper left the pure diffraction contrast pattern ($C_s = 0$, $\Delta = 0$) is shown for a systematic comparison. In order to illustrate that microscope aberrations may increasingly control the image, the loop diameter $d$ (and the corresponding image size) was varied, from left to right, from 12 through 6 to 3 nm approaching the resolution limit of the microscope. The actual Scherzer contrast transfer function ($U = 100$ kV, $C_s = 5.1$ nm, $\Delta = 0$ and 150 nm) causes characteristic fringes, similar to Fresnel fringes to appear along lines of strong contrast changes. This effect becomes most dominant for $d = 3$ nm, where a rapidly oscillating part of the contrast transfer function contributes to the final image.

Fig. 4 displays the bright-field contrast of a straight part of a grain boundary in gold (beam direction $\boldsymbol{e} = [001]$). The model of the grain boundary (direction $[\bar{1}30]$) consists of dislocations seen end-on in pile-up configuration with Burgers vectors of $\boldsymbol{b}_{1,3} = \frac{1}{2}[100]$ and $\boldsymbol{b}_{2,4} = \frac{1}{2}[1\bar{1}0]$. This Au foil of 13.5 nm thickness is tilted in such a way that the diffraction vector $\boldsymbol{g} = (020)$ is exactly excited ($w = 0$). The diffraction contrast ($I_{\text{prim}}$ is the intensity of the bright-field amplitude) is imaged in the upper left of the figure. In the lower left the corresponding diffraction pattern is shown (only the direct (000) reflection has significant intensity) for two different apertures ($\alpha = 0.01$, 0.02 rad). Both these different cut-off diameters of the Scherzer contrast transfer function ($V = 100$ kV, $C_s = 1.4$ nm, $\Delta = 50$ and 90 nm) in Fourier space illustrate the significant influence of its strongly oscillating part of higher frequencies whereby the defocus spread is neglected for this series. The number, the contrast, and the spacing of the "Fresnel fringes" characterize the out-of-focus diffraction contrast. Relative phase rotations caused by aberrations are lowest for $\Delta = 90$ nm and $\alpha_1 = 0.01$ rad, which results in only weak distortions of the image. The contrast features of the bright-field image of the grain boundary (Fig. 4) can be described to a good approximation by applying the lattice rotation model of the dislocations seen end-on. On the other hand, this displacement field model is not sufficient for generating terminated fringes, which are to be expected for lattice fringe contrast (cf. Fig. 2f). The latter results from insufficient surface relaxation caused by the lattice rotation model.

### *3.2 Lattice fringes*

The application of the technique of calculating lattice fringe contrast near crystal defects is illustrated in Fig. 5. For a Ge specimen of 11 nm thickness ($\xi_g/4$) bright-field (BF) and dark-field (DF) diffraction contrasts are computed for a screw dislocation having an inclination of 30° ($\boldsymbol{b} = \frac{1}{2}[011]$). The assumed incident beam direction is $\boldsymbol{e} = [\bar{1}10]$ and the diffraction vector is $\boldsymbol{g} = (111)$. For the computation of the lattice fringe contrast (LF) the interference of the bright-field and dark-field amplitudes

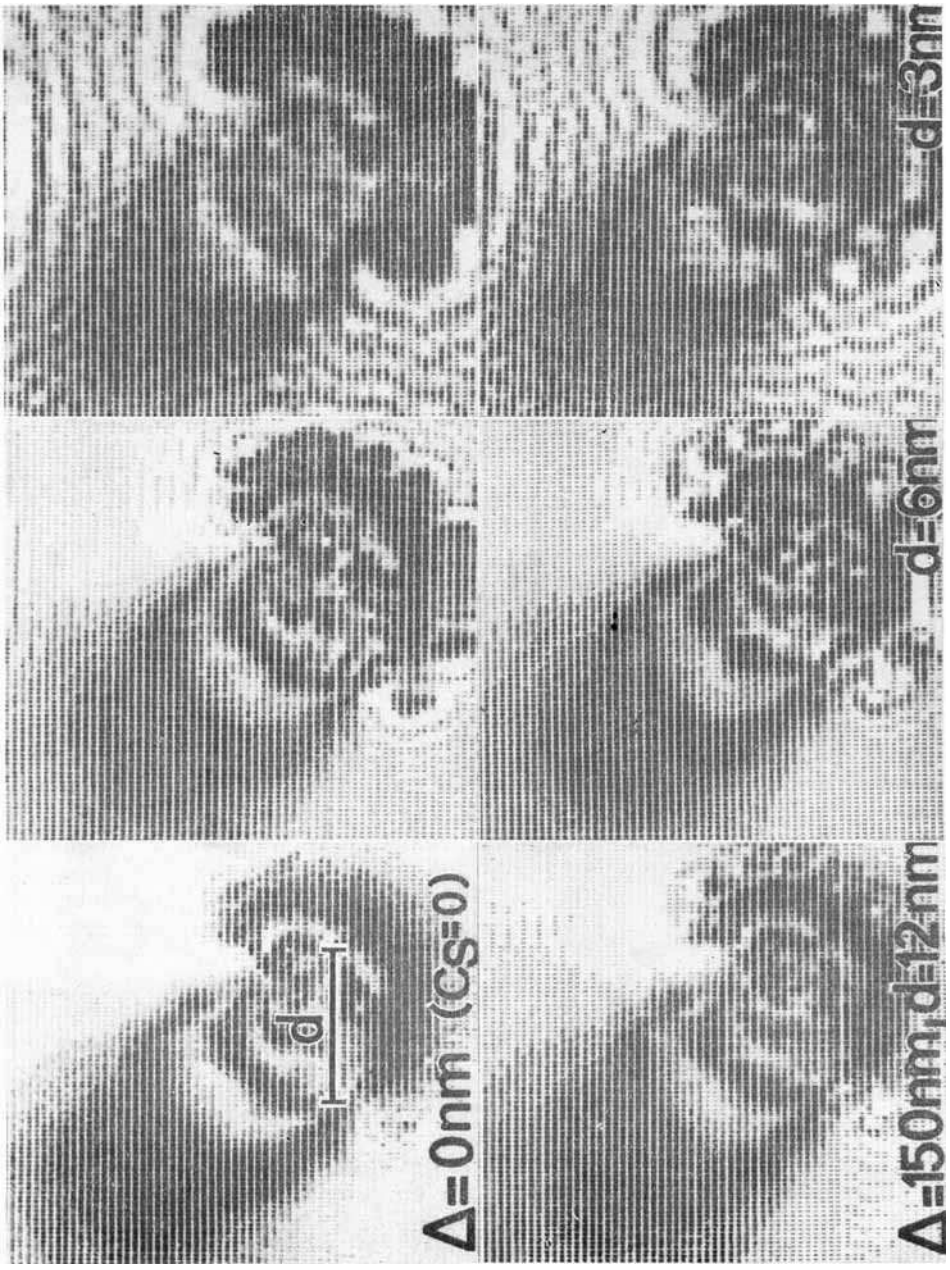


Fig. 3. Influence of the microscope aberrations on the bright-field image of a hexagonal dislocation loop with different loop diameters $d$ and two defocus values $\Delta$ Parameters: $\boldsymbol{g} = (002)$, $\boldsymbol{b} = \frac{1}{3}(11\bar{1})$ $\boldsymbol{e} = [110]$, $\boldsymbol{n} = [11\bar{1}]$, $w = 0$; $U = 100$ kV, $C_s = 5.1$ mm

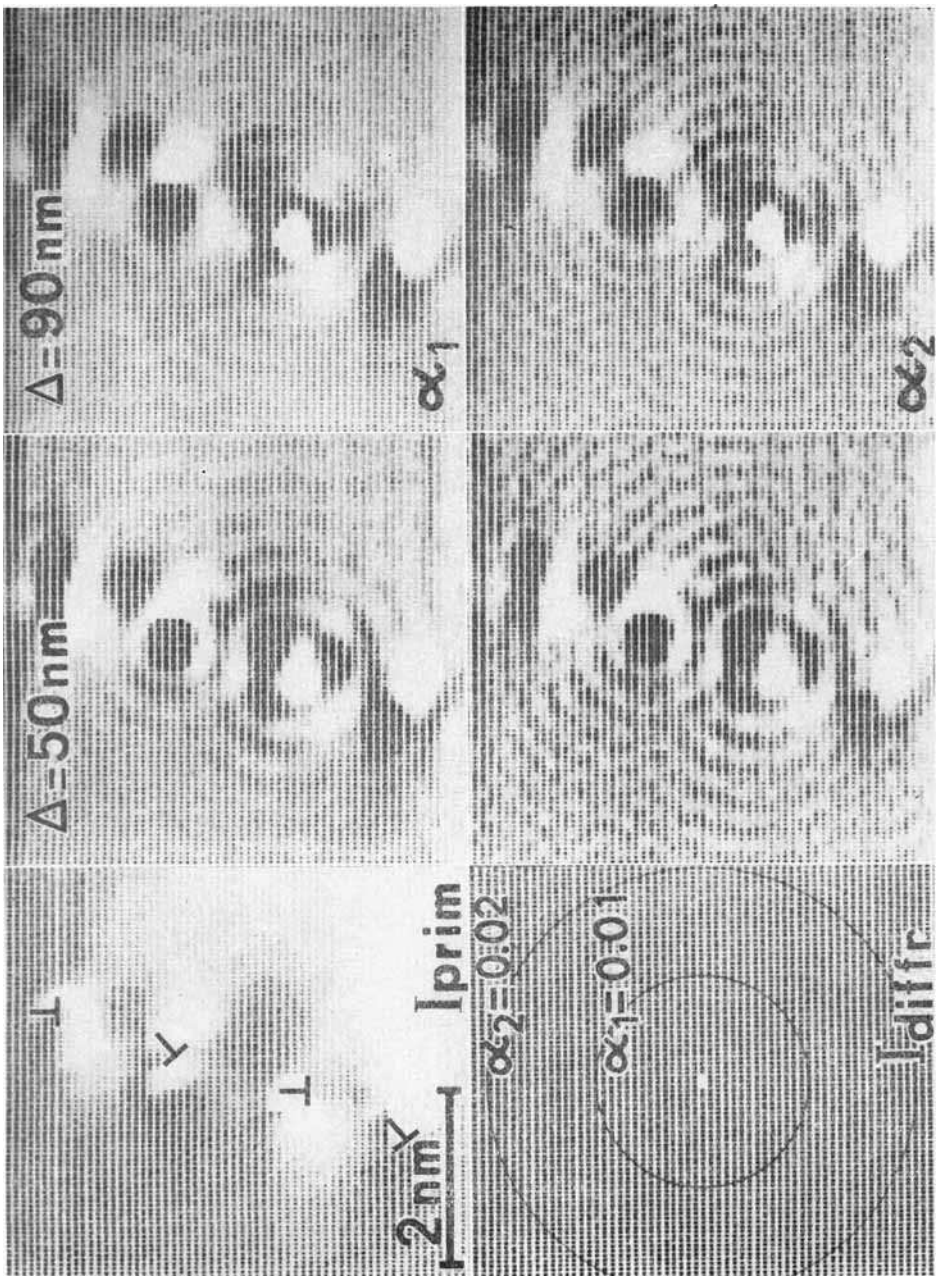


Fig. 4. Influence of defocus $\Delta$ and aperture $\alpha$ on the bright-field contrast of a grain boundary along $[\bar{1}30]$. Parameters: $\boldsymbol{g} = (020)$, $\boldsymbol{b}_1 = \boldsymbol{b}_3 = \frac{1}{2}[100]$, $\boldsymbol{b}_2 = \boldsymbol{b}_4 = \frac{1}{2}[1\bar{1}0]$, $\boldsymbol{e} = [001]$, $w = 0$, $t = 3/4\xi_g$ ($\xi_g$ of Au); $U = 100$ kV, $C_s = 1.4$ mm ($I_{prim}$, $I_{diffr}$ are the ideal image $\Delta = C_s = 0$ and the calculated diffraction pattern, respectively)

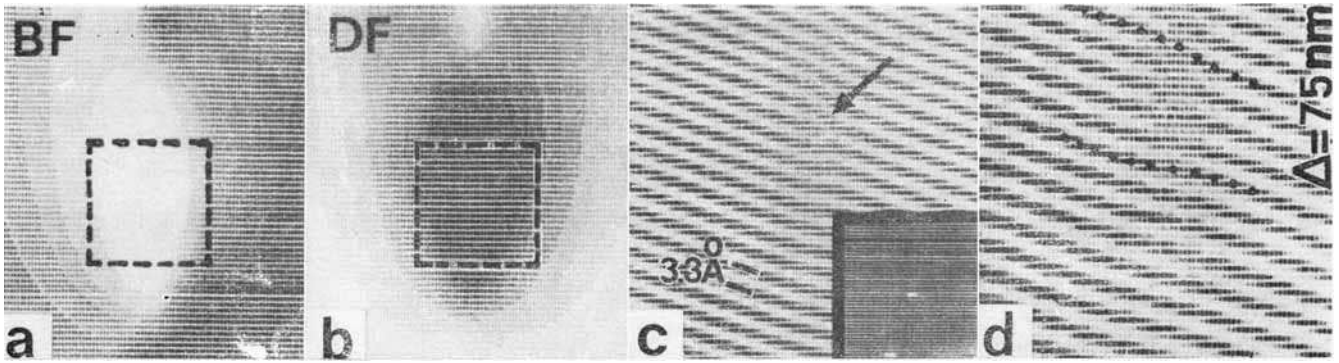


Fig. 5. Bright-field (BF), dark-field (DF), and lattice fringe images of an inclined screw dislocation along [011] direction. Parameters: $\boldsymbol{g} = (111)$, $\boldsymbol{b} = \frac{1}{2}[011]$, $\boldsymbol{e} = [\bar{1}10]$, $w = 0$, $t = \xi_g/4$, ($\xi_g$ of Ge); $U = 100$ kV; a) to c) $C_s = \Delta = 0$; d) $C_s = 1.4$ mm, $\Delta = 75$ nm

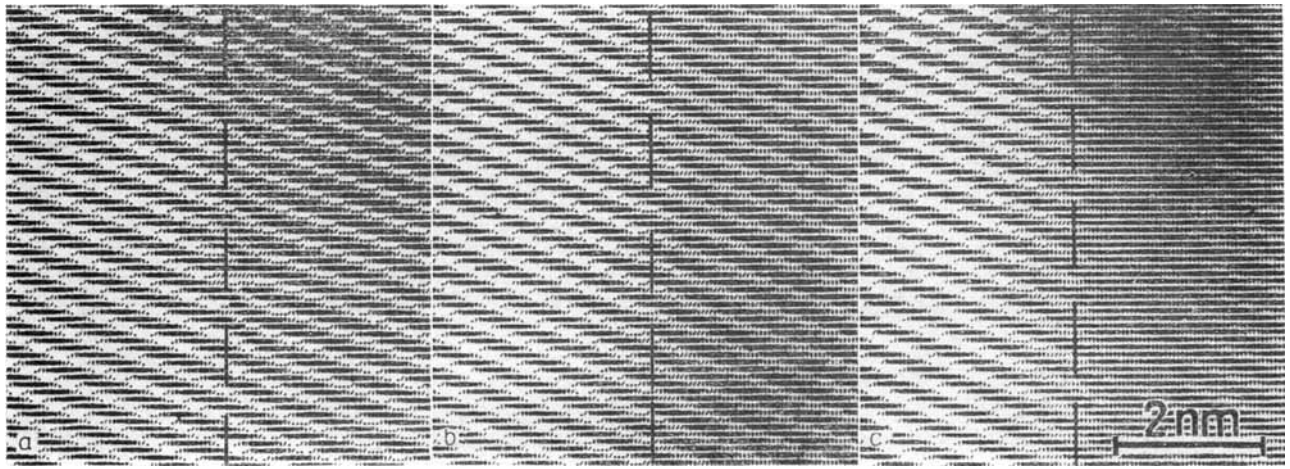


Fig. 6. Calculated lattice fringe patterns of the inclined dislocation of Fig. 5 with a) dislocation direction $[\bar{4}51]$, b) $t = \xi_g/2$, c) $t = 3/4\xi_g$ (for all other parameters cf. Fig. 5)

was carried out according to (4). The marked sub-units of the BF and DF were treated by applying the above interpolation procedure. The inset of the LF image shows the corresponding diffraction pattern. Confirming the $\boldsymbol{g} \cdot \boldsymbol{b}$ criterion ($\boldsymbol{g} \cdot \boldsymbol{b} = 1$) an additional, terminated lattice fringe appears. If, furthermore, the experimental contrast transfer function is taken into account ($U = 100$ kV, $C_s = 1.4$ mm, $\Delta = 75$ nm), the lattice fringe contrast is modified. In the case of this screw dislocation, for instance, it is not possible to localize the terminated fringe, because the contrast is blurred by microscope aberrations. Examples of varying selected specimen parameters of the screw dislocation (cf. Fig. 5) in Ge are shown in Fig. 6. In the left part of Fig. 6 the inclination angle of the dislocation, reaches 64°, whereas the specimen thickness $t = \xi_g/4 = 11$ nm remains constant. Along the trace of the crystal defect, which turns from top to bottom in the middle of the image (see dashed line), there are two significant distortions of the lattice fringe contrast in form of bendings and terminating fringes. An increase of inclination of the dislocation line up to 80° or 90° does not result in disturbed lattice fringes in the present calculations, because the relaxation is not sufficiently described by a lattice rotation model as discussed above (Fig. 4). In the centre and in the right-hand part of Fig. 6 the specimen thickness is varied from $t = 0.5\xi_g$ to $t = 0.75\xi_g$ for the screw dislocation having an inclination of 30° (compare Fig. 5). While the interference pattern for $t = \xi_g/2$ does not show any significant effect, for $t = 0.75\xi_g$ the lattice fringes on either side of the dislocation trace are relatively shifted. The effect of darkening the right-hand side of the screw dislocation has increased.

Fig. 7 shows the interaction of the lattice fringe contrast with thickness fringes of a wedge-shaped specimen (e.g. one edge of a small Au tetrahedron of about 70° wedge angle). The direction of the incident beam is [110] and the diffraction vector is $\boldsymbol{g} = (1\bar{1}\bar{1})$. The orientation of both the crystal edge and the thickness fringes is [1$\bar{1}$0] (see upper left of Fig. 7). In the image field the BF–DF interference pattern is arranged in such a way that all essential numerical effects become obvious. The calculation of the ideal lattice fringe image ($\Delta = 0$, $C_s = 0$) closely confirms the analytical results of (9). The lattice fringe displacement is controlled by the increasing specimen thickness, whereby the periodic lattice fringe shifting is caused by the phase discontinuties of the thickness extinction contours. The influence of the aberrations, which cannot be investigated readily by analytical methods is considered here assuming two types of contrast transfer. In the upper row the CTF is approximated by a simple binary aperture function. The aperture angle decreases from left to right from 0.026 rad (ideal image, because the corresponding point spread function is a $\delta$-function) through 0.017 to 0.014 rad. Overlapping sections (end effect) occur as a result of this aggravating truncation in Fourier space of the boundary of the final image. For an aperture of $\alpha = 0.014$ rad the diffracted beam (DF) is excluded from the image formation, and the lattice fringe contrast vanishes. At the bottom of Fig. 7 for the same decreasing aperture values an actual Scherzer contrast transfer function ($U = 100$ kV, $C_s = 1.4$ mm, $\Delta = 51$ nm) is applied. According to the strongly oscillating CTF in the Fourier space there is a drastic overlapping of periodically succeeding image regions. For decreasing aperture ($\alpha = 0.014$) the CTF approaches unity, and the truncation supersedes the convolution effect of the corresponding, far-reaching, point-spread function of the Scherzer terms.

In order to study the aberrational effect in lattice fringe imaging a through-focus series of a two-beam image for a hexagonal dislocation loop is calculated in Fig. 8. For the given specimen orientation, the incident beam direction is [110] and the diffraction vector is $\boldsymbol{g} = (1\bar{1}1)$. The prismatic crystal defect itself may be characterized by the loop normal $\boldsymbol{n} = [11\bar{1}]$ and the loop diameter of $d = 0.15\xi_g$, the foil thickness

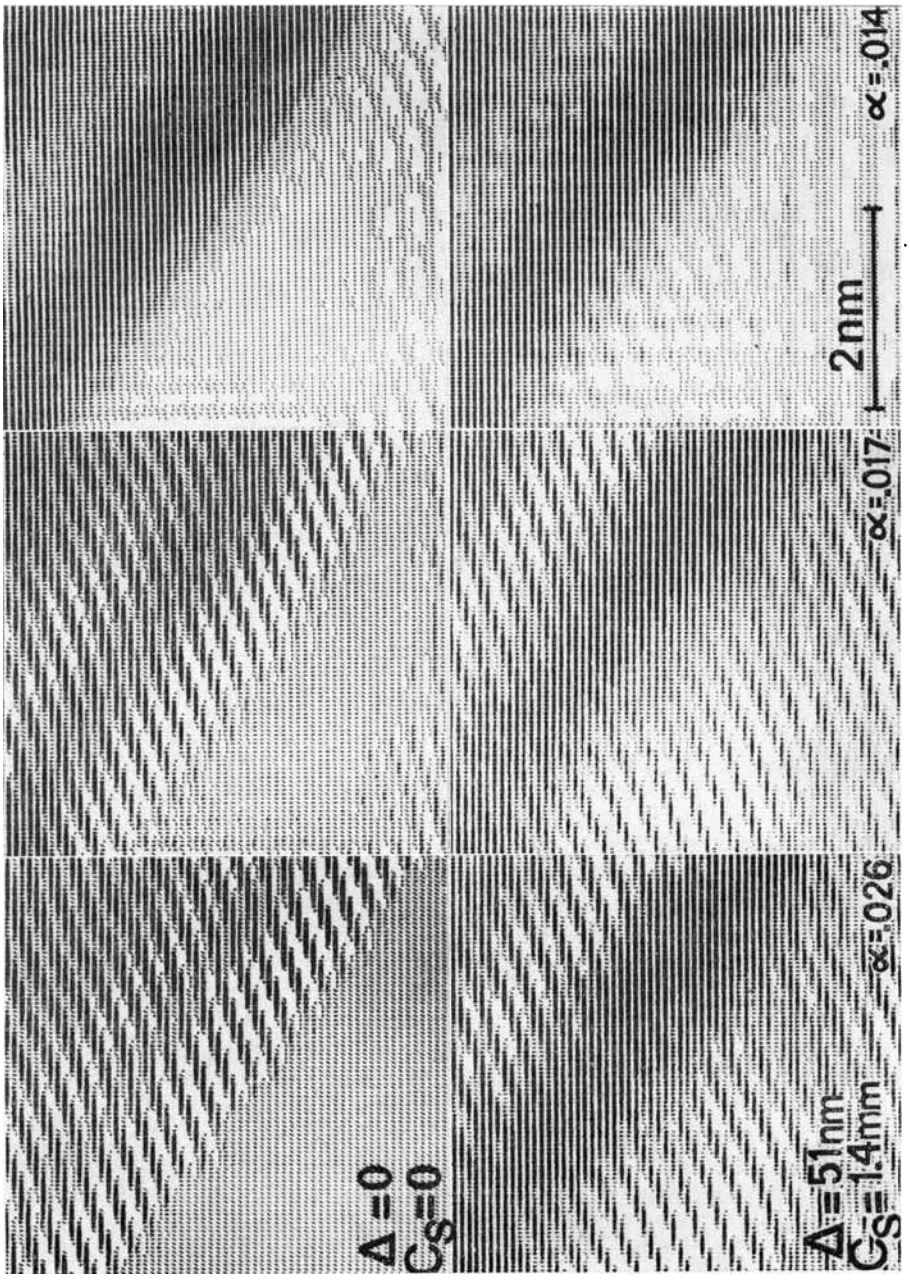


Fig. 7. Interaction of lattice fringes with thickness extinction contours at a wedge-shaped crystal for ideal, $\Delta = C_s = 0$, and aberrated imaging conditions, $\Delta = 51$ nm, $C_s = 1.4$ mm, using different apertures $\alpha$. Parameters: $\boldsymbol{g} = (1\bar{1}1)$, $\boldsymbol{e} = [110]$, $w = 0$ ($\xi_g$ of Au)

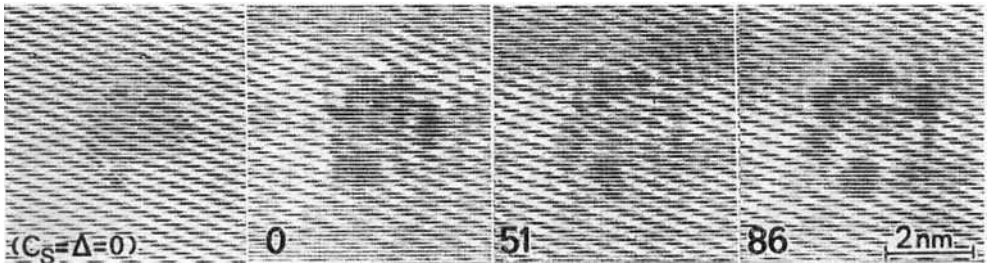


Fig. 8. Through-focus series ($\Delta$) of lattice fringes of a hexagonal dislocation loop. Parameters: $\boldsymbol{g} = (1\bar{1}1)$, $\boldsymbol{b} = \frac{1}{3}[\bar{1}\bar{1}1]$, $\boldsymbol{e} = [110]$, $\boldsymbol{n} = [11\bar{1}]$, $t_0 = 0.625\xi_g$, $t = 1.125\xi_g$ ($\xi_g$ of Au), $w = 0$; $U = 100$ kV, $\alpha = 0.017$ rad, $C_s = 1.4$ mm. Ideal image $C_s = \Delta = 0$ (for comparison)

is $t = 1.125\xi_g$ and the depth position of the loop is $t_0 = 0.625\xi_g$. On the left hand-side of Fig. 8 the ideal interference pattern of bright- and dark-field amplitudes ($C_s = \Delta = 0$) is shown. For the through-focus series the electron microscope imaging parameters are $U = 100$ kV, $C_s = 1.4$ mm, $\Delta = 0, 51, 86$ nm, and $\alpha = 0.017$ rad. The influence of the contrast transfer function emphasizes the residual diffraction contrast of the loop. Characteristic distortions of the lattice fringes remain detectable also for realistic imaging conditions. The positions of the lattice fringe distortions, e.g. bendings and terminated fringes, are marked by dark, blurred contrast details for all defocus values. For $\Delta = 0$ and, especially, for a defocus of $\Delta = 51$ nm Fresnel fringes occur, whereas for the Scherzer focus ($\Delta = 86$ nm) the relative phase rotations are minimal over a wide band of spatial frequencies. In fact, the microscope aberrations seem to cause a slight brightening of the surrounding of the defect.

## 4. Conclusions

Extending the conventional diffraction contrast technique, which as a routine method is used to investigate extended crystal defects, the imaging of small lattice distortions (transition from diffraction contrast to HREM) requires the consideration of the electron microscope aberrations. The computer simulation of defocus diffraction contrast as well as of lattice fringe images of crystal defects has been carried out to demonstrate the importance of contrast transfer for the interpretation of experimental images. For the efficient calculation of the image intensities an appropriate technique of interpolating the complex diffraction amplitudes has been derived. The two stages of the simulation procedure (specimen interaction by diffraction theory, electron-optical imaging process by Fourier formalism) provide interpretable results to be expected for both the defocus diffraction contrast and the lattice fringe patterns. Lattice fringe distortions (including shifting, bending, and termination) are shown to be controlled by phase differences between bright-field and dark-field amplitudes. The examples selected of simulated defect images also allow a critical discussion of numerical problems, e.g. of aliasing and truncation of the discrete Fourier transform and convolution. The computed two-dimensional patterns display additional contrast features in diffraction contrast (e.g. Fresnel fringes) as well as a blurring effect and further fringe modifications for lattice fringe images caused by the microscope contrast transfer.

***Acknowledgements***

The authors wish to thank Prof. T. Mulvey and Prof. J. Heydenreich as well as Dr. V. A. Chamrov for useful discussions.

## Appendix

### *A. Approximation of contrast transfer*

(i) Equation (6) is equivalent to (12) to (14) for the CTF of (13) applied (convolution theorem). For perfect crystals of constant thickness $t$ the amplitudes $\Phi_g(\boldsymbol{R}, t)$ are constant and (4), (12) yield the discrete Fourier spectrum

$$\psi_d(\boldsymbol{\varrho}) = \sum_g \Phi_g \delta(\boldsymbol{g} - \boldsymbol{\varrho}) . \tag{A1}$$

Neglecting $E(\boldsymbol{\varrho})$ and identifying $\boldsymbol{g} = (000)$ with the optical axis for the sake of simplicity, (13), 14) yield

$$\psi_i(\boldsymbol{R}) = \sum_g \Phi_g A(\boldsymbol{g})\, e^{-i\chi(\boldsymbol{g})+2\pi i\boldsymbol{g}\boldsymbol{R}} . \tag{A2}$$

This is equivalent to (8) when applying (5) and using $A(\boldsymbol{g})$ equal to 1 or 0 inside and outside the aperture, respectively.

(ii) For nearly perfect crystals with weakly oscillating $\Phi_g(\boldsymbol{R}, t)$ the distributions in (A1) are spread, but $\psi_d(\boldsymbol{\varrho})$ is different from zero only in small distances $\boldsymbol{\varepsilon}_g$ from the reflections $\boldsymbol{\varrho} = \boldsymbol{g} + \boldsymbol{\varepsilon}_g$. Thus (A2) can be approximated by

$$\psi_i(\boldsymbol{R}) = \sum_g \int \psi_d(\boldsymbol{g} + \boldsymbol{\varepsilon}_g)\, A(\boldsymbol{g} + \boldsymbol{\varepsilon}_g)\, e^{-i\chi(\boldsymbol{g}+\boldsymbol{\varepsilon}_g)}\, e^{2\pi i(\boldsymbol{g}+\boldsymbol{\varepsilon}_g)\boldsymbol{R}}\, d\boldsymbol{\varepsilon}_g \tag{A3}$$

which enables us to extend the approximation of $\chi(\boldsymbol{g})$ given in [7] to complete CTF and arbitrary reflections. While [7] is only applicable to $g \approx 0$ (or also to $g \approx \sqrt{2\Delta/C_s\lambda^3}$ when $C_s$ is included) the approximation up to the second order in $\varepsilon_g^2$

$$e^{-i\chi(\boldsymbol{g}+\boldsymbol{\varepsilon}_g)} \approx e^{-i\chi(\boldsymbol{g})}\{1 - \pi\lambda_i[\Delta(2\boldsymbol{g}\boldsymbol{\varepsilon}_g + \varepsilon_g^2) - C_s\lambda^3(2g^2\boldsymbol{g}\boldsymbol{\varepsilon}_g + g^2\varepsilon_g^2 + 2(\boldsymbol{g}\boldsymbol{\varepsilon}_g)^2)]\} \tag{A4}$$

holds for the general case. With the help of $\nabla$ operating on $\boldsymbol{R}$ (A3), (A4) yield

$$\psi_i(\boldsymbol{R}) = \sum_g A(\boldsymbol{g})\, e^{2\pi i\boldsymbol{g}\boldsymbol{R}-i\chi(\boldsymbol{g})}\left\{1 + \frac{\lambda i}{4\pi}[\Delta(\nabla^2 + 4\pi i\boldsymbol{g}\nabla) - C_s\lambda^3(g^2\nabla^2 + 2(\boldsymbol{g}\nabla)^2 - \right.$$
$$\left. + 4\pi i g^2(\boldsymbol{g}\nabla))]\right\}\Phi_g . \tag{A5}$$

(iii) In analogy to [7] (A5) is specified to diffraction contrast assuming that $A(\boldsymbol{g})$ surrounds only reflection $\boldsymbol{g}$, replacing $\Phi_g$ by (5) and comparing (A5) with the first-order approximation of (9a), i.e. $I_g^{CTF} = I_g + q(\boldsymbol{R})\, I_g + \nabla I_g\, \boldsymbol{\delta}(\boldsymbol{R})$. Denoting further the projection of nabla in the direction of reflection $\boldsymbol{g}$ by $\nabla_g = (\boldsymbol{g}/g)\boldsymbol{g}/g\nabla)$ one obtains

$$\begin{aligned} q(\boldsymbol{R}) &= -\frac{\lambda\Delta}{2\pi}\nabla^2\varphi + \frac{C_s\lambda^4 g^2}{2\pi}(\nabla^2\varphi + \nabla_g^2\varphi) , \\ \boldsymbol{\delta}(\boldsymbol{R}) &= -\frac{\lambda\Delta}{2\pi}(2\pi\boldsymbol{g} + \nabla\varphi) + \frac{C_s\lambda^4 g^2}{2\pi}(2\pi\boldsymbol{g} + \nabla\varphi + 2\nabla_g\varphi) . \end{aligned} \tag{A6}$$

For $g = 0$ (A6) confirms [7]. Furthermore, $E(\boldsymbol{\varrho})$ can be included by a damping factor and a tilt of the optical axis can be considered by a shift of $\boldsymbol{g}$.

### *B. Approximation of diffraction contrast*

(i) Equation (1) for the two-beam case $(0, \boldsymbol{g})$ can be written

$$\Phi_0' = \pi i \sigma_0 \Phi_g\,, \qquad \Phi_g' = 2\pi i(s_g + \beta_g')\,\Phi_g + \pi i \sigma_0 \Phi_0\,, \tag{A7}$$

whereby $\sigma_0 = 1/\xi_g + i/\xi_g'$. Using (5) one obtains

$$\begin{aligned} \delta\varphi' &= 2\pi(s_g + \beta_g') + \frac{\pi}{\xi_g}\cos\delta\varphi\left(\frac{T_0}{T_g} - \frac{T_g}{T_0}\right) + \frac{\pi}{\xi_g'}\sin\delta\varphi\left(\frac{T_0}{T_g} + \frac{T_g}{T_0}\right), \\ T_{0,g}' &= -\pi T_{g,0}\left(\frac{1}{\xi_g}\sin\delta\varphi \pm \frac{1}{\xi_g'}\cos\delta\varphi\right), \end{aligned} \tag{A8}$$

which in first-order approximation immediately results in (11).

(ii) The solution of (A7) for perfect crystals of thickness $t$ is given by

$$\Phi_0 = \left(\cos\pi\sigma t - \frac{i s_g}{\sigma}\sin\pi\sigma t\right)\mathrm{e}^{\pi i s_g t}\,, \qquad \Phi_g = \frac{i\sigma_0}{\sigma}\sin\pi\sigma t\,\mathrm{e}^{\pi i s_g t} \tag{A9}$$

with $\sigma = \gamma + i\tau = \sqrt{\sigma_0^2 + s_g^2}$. Using (5) one obtains

$$\begin{aligned} I_0 &= \frac{1}{2(\gamma^2 + \tau^2)}[(\gamma^2 + \tau^2 + s_g^2)\cosh 2\pi\tau t + (\gamma^2 + \tau^2 - s_g^2)\cos 2\pi\gamma t - \\ &\quad - s_g\gamma \sinh 2\pi\tau t - s\tau \sin 2\pi\gamma t]\,, \\ I_g &= \frac{1}{2}\frac{\xi_g^{-2} + \xi_g'^{-2}}{\gamma^2 + \tau^2}(\cosh 2\pi\tau t - \cos 2\pi\gamma t)\,, \end{aligned} \tag{A10}$$

$$\cot\delta\varphi = \frac{(\tau/\xi_g - \gamma/\xi_g')\sin 2\pi\gamma t - (\gamma/\xi_g + \tau/\xi_g')\sinh 2\pi\tau t - (s/\xi_g)(\cosh 2\pi\tau t - \cos 2\pi\gamma t)}{(\gamma/\xi_g + \tau/\xi_g')\sin 2\pi\gamma t + (\tau/\xi_g - \gamma/\xi_g')\sinh 2\pi\tau t + (s/\xi_g')(\cosh 2\pi\tau t - \cos 2\pi\gamma t)}.$$

Neglecting absorption $1/\xi_g' = 0$, (10) is directly obtained. A further well-established approximation is given by $\gamma = (1/\xi_g)\sqrt{1 + w^2}$ and $\tau = \xi_g/\xi_g'\sqrt{1 + w^2}$.

### *C. Interpolation*

The formulas

$$\Phi_{\mathrm{MP}}(x) = \left[T_1 + (T_2 - T_1)\frac{x - x_1}{x_2 - x_1}\right]\mathrm{e}^{i\left[\varphi_1 + (\varphi_2 - \varphi_1)\frac{x - x_1}{x_2 - x_1}\right]} \tag{A11}$$

and

$$\Phi_{\mathrm{RI}}(x) = \Phi_1 + (\Phi_2 - \Phi_1)\frac{x - x_1}{x_2 - x_1} \tag{A12}$$

characterize the independent interpolation in modulus and phase (MP), or real and imaginary parts (RI) of a complex function $\Phi(x)$ given at the pivot points $\Phi_j = \Phi(x_j) = T_j\,\mathrm{e}^{i\varphi_j}$ (without loss of generality one-dimensional arguments are used; the bilinear interpolation as well as the questions of the order of interpolation and the selection of pivot points are directly related to properties of the discrete convolution and will be outlined otherwise). While the interpolated phase of (A11) levels the discontinuities, the latter are reproduced by

$$\varphi_{\mathrm{RI}} = \arctan\frac{T_1\sin\varphi_1(x_2 - x) + T_2\sin\varphi_2(x - x_1)}{T_1\cos\varphi_1(x_2 - x) + T_2\cos\varphi_2(x - x_1)}, \tag{A13}$$

which is the resulting phase of (A12). Comparing the resulting interpolated moduli one obtains

$$T_{\mathrm{RI}}^2 - T_{\mathrm{MP}}^2 = 2T_1T_2\,[\cos(\varphi_2 - \varphi_1) - 1]\,\frac{(x_2 - x)\,(x - x_1)}{(x_2 - x_1)} \tag{A14}$$

showing the maximal difference at discontinuity $\varphi_1 - \varphi_2 = \pm\pi$ of phases.

## References

[1] G. R. ANSTIS and D. J. H. COCKAYNE, Acta cryst. **A35**, 511 (1979).
[2] W. GRUSCHEL, A. LAUPHEIMER, and M. WILKENS, Electron Microscopy 1982, Proc. 10th Internat. Congr. Electr. Microsc., Vol. 2, Hamburg 1982 (p. 97).
[3] M. WILKENS, Electron Microscopy 1984, Proc. 8th Europ. Congr. Electr. Microsc., Vol. 1, Budapest 1984 (p. 175).
[4] K. SCHEERSCHMIDT and R. HILLEBRAND, Proc. 11th Hung. Diffr. Conf., Györ 1982 (p. 126).
[5] K.-H. KATERBAU, phys. stat. sol. (a) **59**, 211 (1980); Phil. Mag. **A43**, 409 (1981).
[6] N. I. BORGARDT, S. K. MAKSIMOV, and D. I. PISKUNOV, phys. stat. sol. (a) **86**, 55 (1984).
[7] V. A. CHAMROV, V. L. INDENBOM, and I. A. RUSAKOVA, see [3] (p. 335).
[8] A. HOWIE and Z. S. BASINSKI, Phil. Mag. **17**, 1039 (1968).
[9] P. B. HIRSCH, A. HOWIE, R. B. NICOLSON, D. W. PESHLEY and M. J. WHELAN, Electron Microscopy of Thin Crystals, Butterworths, London 1965.
[10] K. SCHEERSCHMIDT and J. HEYDENREICH, phys. stat. sol. (a) **42**, 47 (1977).
[11] R. HILLEBRAND, K. SCHEERSCHMIDT, W. NEUMANN, P. WERNER, and A. PIPPEL, Bildinterpretation in der Hochauflösungselektronenmikroskopie, Akademie-Verlag, Berlin 1984.
[12] M. MANNAMI, J. Phys. Soc. Japan **17**, 1160 (1962).
[13] W. J. TUNSTALL, P. B. HIRSCH, and J. STEEDS, Phil. Mag. **9**, 99 (1964).
[14] D. K. SALDIN and M. J. WHELAN, Phil. Trans. Roy. Soc. (London) **A292**, 53 (1979).
[15] S. K. MAKSIMOV and N. I. BORGARDT, phys. stat. sol. (b) **119**, 685 (1983).
[16] P. R. SMITH, Ultramicroscopy **6**, 201 (1981).

*(Received August 15, 1985)*